

# Boosting the Bifunctionality and Durability of Cobalt-Fluoride-Oxide Nanosheets for Alkaline Water Splitting Through Nitrogen-Plasma-Promoted Electronic Regulation and Structural Reconstruction

Shuo Wang,<sup>#</sup> Cheng-Zong Yuan,<sup>#</sup> Yunshan Zheng,<sup>#</sup> Yao Kang, Kwan San Hui,<sup>\*</sup> Kaixi Wang, Haixing Gao, Duc Anh Dinh, Young-Rae Cho,<sup>\*</sup> and Kwun Nam Hui<sup>\*</sup>



Cite This: *ACS Catal.* 2024, 14, 3616–3626



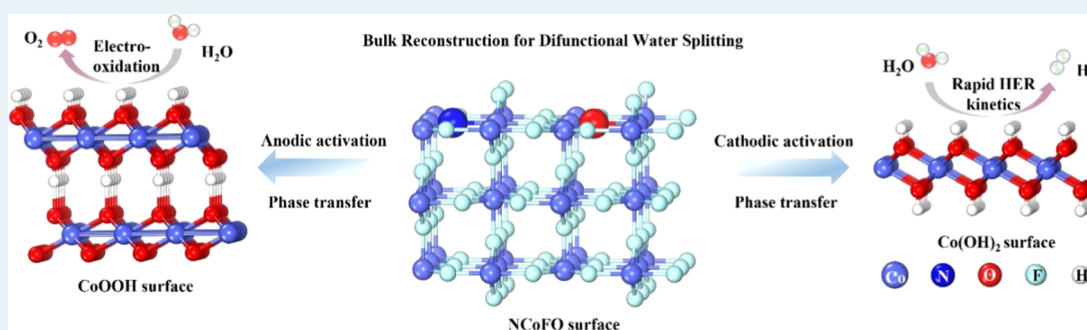
Read Online

ACCESS |

Metrics & More

Article Recommendations

Supporting Information



**ABSTRACT:** Designing cost-effective and durable bifunctional electrocatalysts with high activity for the hydrogen evolution reaction (HER) and oxygen evolution reaction (OER) is crucial for large-scale hydrogen production through water splitting. However, many electrocatalysts undergo surface or bulk reconstruction, leading to an unstable catalytic activity. In this study, we present a facile  $N_2$  plasma strategy to enhance the electrocatalytic activity of cobalt-fluoride-oxide (CoFO, herein NCoFO) nanosheets while maintaining reasonably stable performance. The optimized NCoFO nanosheets grown on carbon cloth through a 60 s  $N_2$  plasma treatment (NCoFO/CC-60) exhibit remarkable performance with low overpotentials of 203 mV and 230 mV at  $10 \text{ mA cm}^{-2}$  for the HER and the OER, respectively. Density functional theory calculations revealed that the enhanced catalytic performance is attributed to the regulated local electronic configuration resulting from plasma treatment. Furthermore, the assembled alkaline electrolyzer NCoFO/CC-60||NCoFO/CC-60 requires an extremely low voltage of 1.48 V to attain  $10 \text{ mA cm}^{-2}$  for over a 150 h operation, which is superior to the values obtained for Pt/Cl||RuO<sub>2</sub> (1.50 V) and CoFO/CC||CoFO/CC (1.55 V).

**KEYWORDS:** metal–fluoride oxides,  $N_2$  plasma, bulk reconstruction, electronic structure reformation, water splitting

## 1. INTRODUCTION

Electrochemical water splitting, powered by renewable energy sources, is a promising method for scalable production of green hydrogen.<sup>1</sup> However, its competitiveness compared to gray hydrogen generation, which relies on coal or natural gas steam reforming, is hindered by high fabrication costs and low efficiency, resulting from sluggish reaction kinetics at both the cathode for the hydrogen evolution reaction (HER) and the anode for the oxygen evolution reaction (OER). To overcome these challenges and enhance energy conversion efficiency, it is crucial to develop efficient and cost-effective electrocatalysts that can accelerate half-reactions at the electrodes. These catalysts play a vital role in advancing the widespread application of water splitting in the hydrogen generation industry. At present, platinum (Pt)- and ruthenium (Ru)-based materials are considered the leading catalysts for the hydrogen evolution reaction (HER) and oxygen evolution reaction (OER), respectively. However, their practical application is

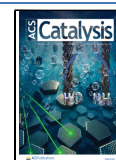
hindered by their scarcity in the Earth's crust and high cost. Therefore, there is significant interest in developing cost-effective nonprecious metal electrocatalysts to address the cost and efficiency challenges associated with water splitting.<sup>2</sup> Typically, different electrocatalysts are used for the HER at the cathode and the OER at the anode due to their distinct reaction mechanisms and pathways. However, the fabrication and maintenance costs can be significantly reduced by developing bifunctional catalysts that can facilitate both reactions. This enables the fabrication of symmetric cells, where the same catalyst material can be used for both the HER

**Received:** January 13, 2024

**Revised:** February 3, 2024

**Accepted:** February 5, 2024

**Published:** February 20, 2024



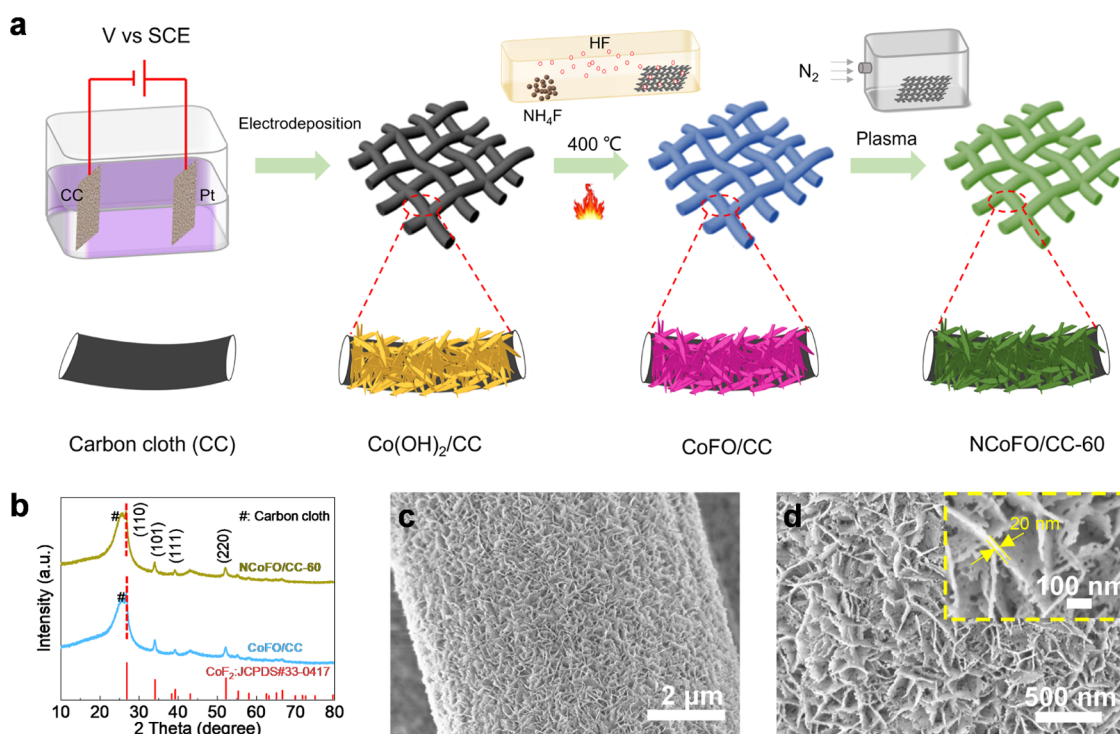


**Figure 1.** (a) Illustration of the fabrication route of NCoFO/CC-60. (b) XRD pattern of CoFO/CC and NCoFO/CC-60 samples. (c, d) SEM images of NCoFO/CC-60 sample (the inset is enlarged SEM images).

and the OER, further enhancing the cost-effectiveness of the water splitting process.

Extensive research efforts have been dedicated to investigating Earth-abundant bifunctional electrocatalysts for efficient water splitting. Various materials have been explored, including transition-metal-based alloys,<sup>3</sup> oxides,<sup>4</sup> phosphides,<sup>5–7</sup> nitrides,<sup>8</sup> heterostructure,<sup>9</sup> and carbonate hydroxides.<sup>10</sup> Among these, cobalt fluoride oxides (CoFO) have emerged as promising candidates due to their excellent electronic conductivity and high activity in the OER. This is attributed to the presence of both Co–O and Co–F bonds, which facilitate electron abstraction from neighboring metals, leading to the availability of abundant coordinatively unsaturated sites.<sup>11,12</sup> The Sabatier principle states that catalysts should establish intermediate-strength bonds with atoms or molecules. Too weak interactions hinder reactant activation, while overly strong interactions impede product desorption.<sup>13</sup> In the case of CoFO, the presence of highly electronegative F and O atoms results in strong binding forces with adsorbed intermediates. This strong binding can lead to a decline in catalytic activity and hinder the utilization of specific active sites.<sup>12,14</sup> To address this issue, the electronic regulation of the active sites through heteroatom doping (N,<sup>15,16</sup> S,<sup>17</sup> O,<sup>18</sup> and Se<sup>19</sup>) has been recognized as a powerful strategy to enhance the intrinsic activity of materials.<sup>16,20</sup> This enhancement arises from the induced subtle lattice distortion and redistribution of electron density at the atomic-level active sites.<sup>18,21</sup> Therefore, incorporating N dopants, which have relatively low electronegativity, offers an opportunity to reconfigure the coordination structure and adjust the electronic density of CoFO.<sup>22</sup>

The plasma treatment method, which offers the advantages of low energy consumption and no chemical waste, has been recognized as an effective and straightforward approach to tune the surface electronic structures of high-performance catalysts

by creating vacancies on the material's surface. Huang et al. utilized an Ar-plasma-assisted strategy to fabricate hierarchical spinel  $\text{Co}_3\text{O}_4$  porous nanoneedle arrays with heteroatom Mo substitution and oxygen vacancies, in situ grown on carbon cloth.<sup>23</sup> This approach significantly improved the OER performance, achieving a low overpotential of only 276 mV at  $10 \text{ mA cm}^{-2}$ . The enhanced OER performance can be attributed to the efficient regulation of the atomic ratio of  $\text{Co}^{3+}/\text{Co}^{2+}$  and the increased number of oxygen vacancies induced by the presence of Mo with variable valence states. Furthermore, another study reported that the monolayer  $\text{MoS}_2$  exhibited a greatly enhanced HER performance after a 20 min  $\text{N}_2$  plasma treatment. The treated  $\text{MoS}_2$  displayed an onset overpotential of approximately 210 mV at  $10 \text{ mA cm}^{-2}$  along with a Tafel slope of approximately 89 mV/dec.<sup>24</sup> However, developing a plasma-based approach to fabricate vacancy-assisted bifunctional electrocatalysts with high performance in both the HER and the OER, while maintaining operational stability, remains a challenge.

Here, we present the development of highly active and durable bifunctional electrocatalysts based on CoFO for both the HER and the OER by employing a facile nitrogen plasma treatment technique to obtain N-doped CoFO (NCoFO) nanosheets (NCoFO). The plasma treatment process simultaneously introduces nitrogen doping into the CoFO lattice and creates fluorine vacancies, effectively regulating the surface electronic structure of the material. The optimized NCoFO nanosheets grown on carbon cloth through a 60 s  $\text{N}_2$  plasma treatment (NCoFO/CC-60) exhibit remarkable performance with low overpotentials of 203 and 230 mV at  $10 \text{ mA cm}^{-2}$  for the HER and the OER, respectively. The altered electronic structure also facilitates bulk reconstruction during electrode reactions, leading to changes in the morphology and composition of the electrocatalyst. Surprisingly, these changes

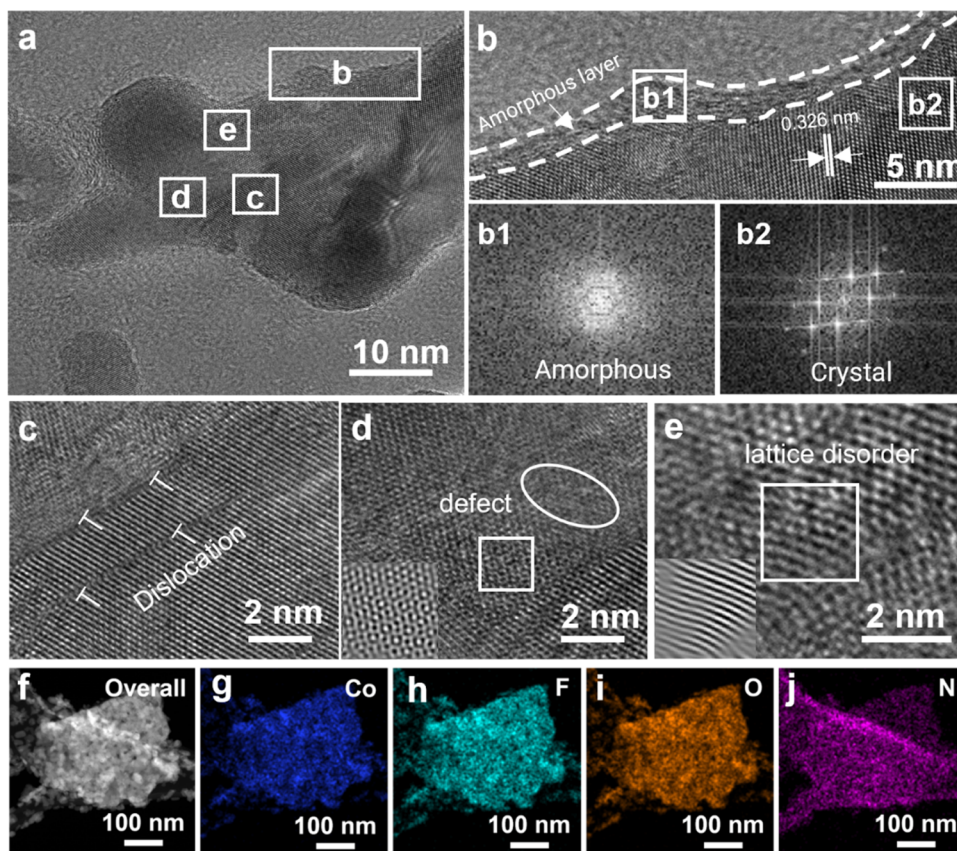


**Figure 2.** (a, b) HRTEM images of NCoFO/CC-60 sample. (c) Numerous dislocations and distortions marked with “T” were observed and retained the original phase arrangement with a nanodomain structure. (d) Defects on the material surface. (e) Lattice disorder of materials, which was attributed to N incorporation. (f–j) EDX mapping of various elements in the porous NCoFO/CC-60 nanosheet.

do not affect the apparent activity for the HER and the OER, resulting in consistent catalytic performance over time. In contrast, the catalytic performance of CoFO without plasma treatment rapidly deteriorates. Therefore, this study introduces a novel strategy for the development of highly active and durable bifunctional electrodes for water splitting. These findings have significant implications for accelerating the commercialization of water splitting technologies and achieving a zero-carbon energy future.

## 2. RESULTS AND DISCUSSION

**2.1. Synthesis of NCoFO/CC.** Figure 1a depicts the two approaches employed to obtain NCoFO porous nanosheets on carbon cloth (NCoFO/CC): vapor fluorination and nitrogen plasma. Initially, hierarchical  $\text{Co}(\text{OH})_2$  nanosheets were electrodeposited onto a carbon cloth. Subsequently, the nanosheets were calcined at 400 °C in an Ar atmosphere for 1 h in the presence of  $\text{NH}_4\text{F}$  powder, generating an HF atmosphere. This conversion process resulted in the formation of CoFO/CC nanosheets. Following the  $\text{N}_2$  plasma treatment, the resulting sample was thoroughly rinsed with deionized (DI) water. Four different plasma durations were employed: 0, 30, 60, and 90 s. The resulting samples were labeled as NCoFO/CC-0, NCoFO/CC-30, NCoFO/CC-60, and NCoFO/CC-90, respectively. A comprehensive set of characterizations was conducted to examine the morphology and crystal structure of the synthesized samples. As shown in Figure S1, the X-ray diffraction (XRD) patterns of the precursor well matched the orthorhombic  $\text{Co}_5(\text{O}_{9.48}\text{H}_{8.52})\text{NO}_3$

structure (JCPDS: 46–0605).<sup>25</sup> After calcination at 400 °C in HF, new diffraction peaks at  $2\theta$  values of 26.7, 34.0, 39.1, 52.0, and 55.1° appeared in the XRD patterns of the CoFO/CC-60 sample (Figure 1b), suggesting the conversion (decomposition) of  $\text{Co}_5(\text{O}_{9.48}\text{H}_{8.52})\text{NO}_3$  precursor into hexagonal  $\text{CoF}_2$ -type phase (JCPDS#33–0417).<sup>26</sup> Compared to the standard XRD pattern of  $\text{CoF}_2$ , both the CoFO/CC and NCoFO/CC-60 samples exhibited no noticeable changes, indicating that the introduction of oxygen and nitrogen atoms did not influence the morphology of  $\text{CoF}_2$ , as they were successfully doped onto its surface. In addition to the electronic structure, the impact of nitrogen plasma treatment on the morphological structure of the samples was also studied. Figure S2 illustrates that the CoFO/CC sample exhibited a hierarchical nanosheet morphology similar to that of the  $\text{Co}(\text{OH})_2/\text{CC}$  precursor. Therefore, the calcination process primarily induced a phase transformation with minimal impact on the morphology. However, notable differences were observed in the surface characteristics between the CoFO/CC nanosheets and the  $\text{Co}(\text{OH})_2/\text{CC}$  precursor. The surface of the CoFO/CC nanosheets appeared significantly rougher, which can be attributed to the dehydration and release of gases from the precursor during the calcination process.<sup>27</sup> No substantial morphological changes were observed in the NCoFO/CC-60 sample (Figure 1c,d) after 60 s of  $\text{N}_2$  plasma treatment when compared to the CoFO/CC counterpart (Figure S2c,d). This observation indicates that the nitrogen plasma treatment did not significantly alter the morphological structure of the samples. Further support for this conclusion was obtained from

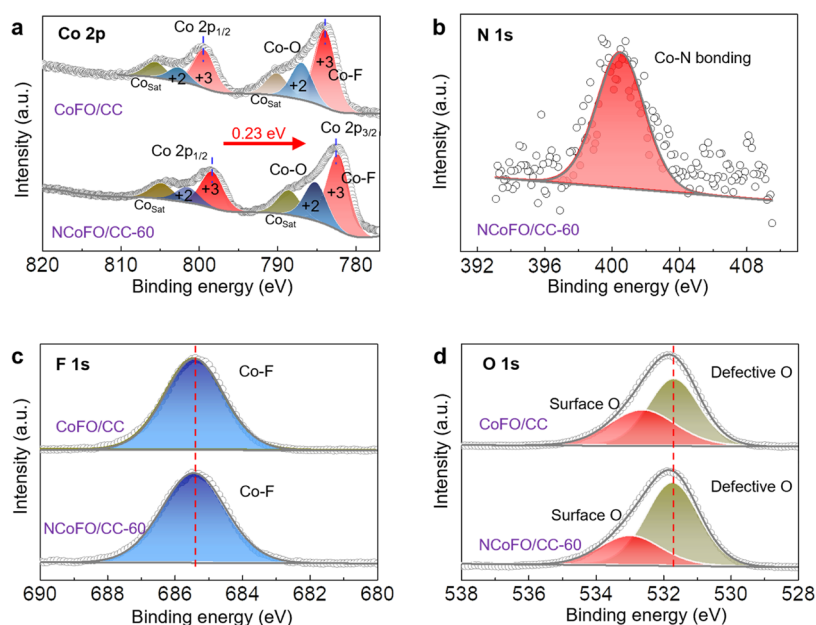


**Figure 3.** XPS spectra of (a) Co 2p, (b) N 1s, (c) F 1s, and (d) O 1s of CoFO/CC (top) and NCoFO/CC-60 (bottom).

the analysis of NCoFO/CC samples subjected to different plasma treatment times, as depicted in Figure S3.

**2.2. Characterizations of Materials.** To gain further insights into the morphology and structural characteristics of NCoFO/CC-60, high-resolution transmission electron microscopy (HRTEM) was employed. The HRTEM analysis, as depicted in Figure S4, clearly displayed distinct contrasts in various regions of the image, providing evidence of the abundant nanoporous structure within the NCoFO/CC-60 nanosheets. The presence of numerous pores in the NCoFO/CC-60 catalyst is advantageous for facilitating efficient mass transfer, which, in turn, is believed to enhance the overall catalytic properties of the material.<sup>28</sup> Figure 2a,b reveals the presence of a partial amorphous layer on the edge of the CoFO nanosheet structure in NCoFO/CC-60, resulting from the N<sub>2</sub> plasma treatment.<sup>29</sup> This amorphous nature is evident from the absence of diffraction rings in the fast Fourier transform (Figure 2b1), contrasting with the clear diffraction dots observed in the CoFO nanosheet area (Figure 2b2). Furthermore, a detailed analysis of the high-resolution transmission electron microscopy (HRTEM) image revealed well-defined lattice fringes with a *d*-spacing of 0.326 nm (Figure 2b). Remarkably, this *d*-spacing corresponds precisely to the (110) diffraction plane of the NCoFO/CC-60 CaF<sub>2</sub>-type phase.

The HRTEM images (Figure 2a–e) revealed an intriguing observation of numerous defects and lattice dislocations within the NCoFO/CC-60 nanosheets. Notably, the nanodomain regions in Figure 2c exhibited a high density of dislocations and distortions, which were conveniently marked with “T”. Furthermore, some locations exhibited distinct defects with noticeable distortions of the lattice fringes, as illustrated in Figure 2d. Considering the subsequent XPS results, these observed defects are likely attributed to the presence of fluorine vacancies (V<sub>F</sub>). The observed defects and dislocations are believed to have originated from the incorporation of extraneous nitrogen, which introduced additional catalytic sites to enhance the reaction kinetics.<sup>6,30</sup> This is supported by the energy-dispersive X-ray spectroscopy (EDX) mapping images

(Figure 2f–j) and compositional line profiles (Figures S5 and S6), which demonstrated the presence of nitrogen (in addition to cobalt, fluorine, and oxygen) uniformly distributed throughout the NCoFO/CC-60 sample. These findings suggest that nitrogen doping occurred, indicating a doping mechanism rather than the formation of a composite material. The influence of nitrogen plasma treatment on the electronic structure of the samples was investigated by using X-ray photoelectron spectroscopy (XPS), and a survey spectrum is provided in Figure S7. The Co 2p core-level spectra of the NCoFO/CC-60 and CoFO/CC samples are displayed in Figure 3a, and the full-width at half-maximum (fwhm) values of Co are listed in Table S1. Two peaks at 782.6 and 797.9 eV were observed, corresponding to the spin-orbit effects of the metallic Co 2p<sub>3/2</sub> and Co 2p<sub>1/2</sub> peaks, respectively.<sup>12,26</sup> Notably, the Co 2p<sub>3/2</sub> peak of NCoFO/CC-60 exhibited a lower binding energy compared to that of CoFO/CC. This shift in the peak position can be attributed to the incorporation of low-electronegativity nitrogen atoms into the CoFO structure. The presence of fewer electrons involved in Co–N bonding, as compared to Co–F bonding, due to the weaker electron-withdrawing ability of nitrogen compared to fluorine, led to a lower oxidation state of cobalt in NCoFO/CC-60.<sup>21,22</sup> Consequently, the incorporation of N dopants effectively regulated the atomic and electronic structure of NCoFO/CC-60.<sup>6,22</sup> A detailed analysis of this phenomenon is further discussed in the theoretical discussion section. The atomic percentages of the fitting peaks corresponding to Co–F and Co–O bonds were calculated (Figure S8a). The observed reduced concentration of Co–F bonding in NCoFO/CC-60 indicated that plasma treatment also led to the formation of V<sub>F</sub> on the surface of the material. This conclusion is further supported by the HRTEM observations (Figures 2a–e and S8b). In the high-resolution N 1s spectra of the NCoFO/CC-60 samples (Figure 3b), the Co–N bond peak at 401.5 eV exhibited a slight negative shift of approximately 0.2 eV compared to that of pure nitrogen.<sup>6,15</sup> This shift confirms the presence of Co–N bonds in NCoFO/CC-60, highlighting the incorporation of nitrogen into the material. The high-

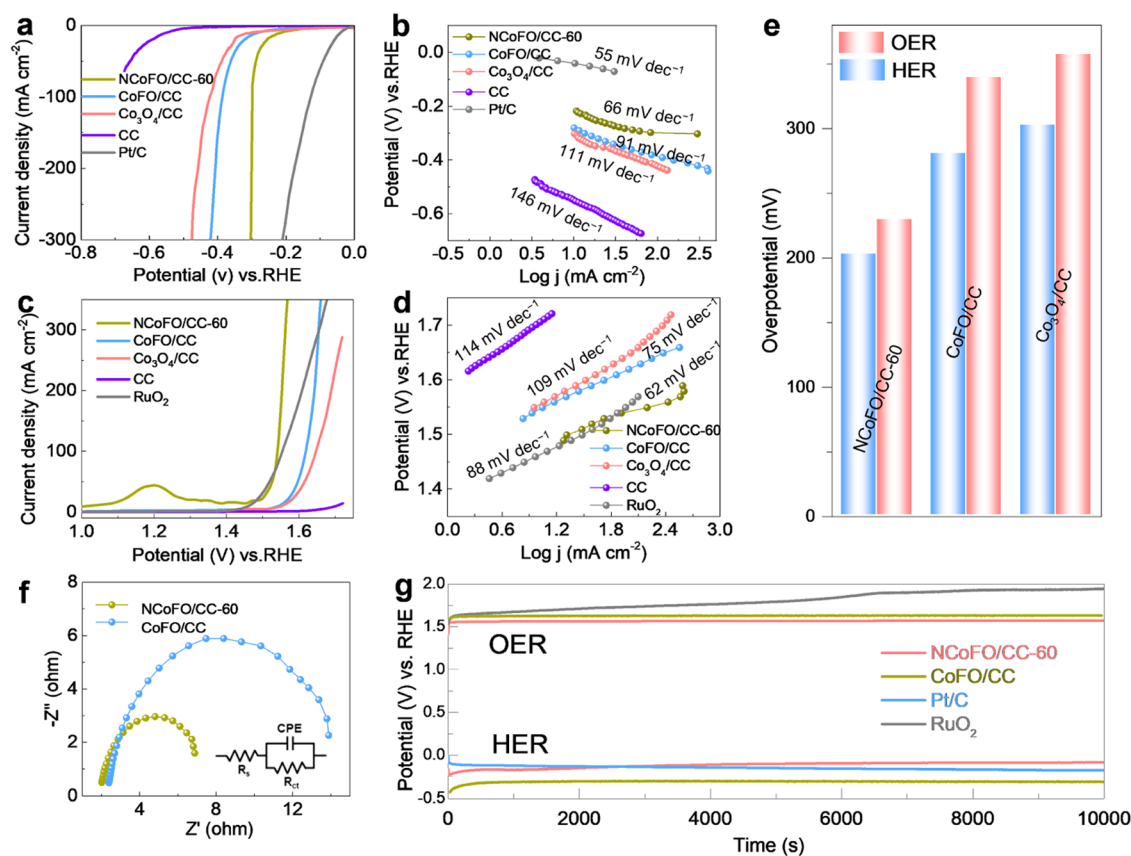


**Figure 4.** (a) LSV curves of NCoFO/CC-60 and the compared samples in 1.0 M KOH solution for HER at a scan rate of  $10 \text{ mV s}^{-1}$ . (b) Corresponding Tafel plots of NCoFO/CC-60 and the compared samples in 1.0 M KOH solution for HER. (c) LSV curves of NCoFO/CC-60 and the compared samples in 1.0 M KOH solution for OER at a scan rate of  $10 \text{ mV s}^{-1}$ . (d) Corresponding Tafel plots of NCoFO/CC-60 and the compared samples in 1.0 M KOH solution for OER. (e) Overpotentials at  $10 \text{ mA cm}^{-2}$  for NCoFO/CC-60 and the compared samples in 1.0 M KOH solution. (f) EIS plots of the NCoFO/CC-60 and CoFO/CC. Inset is the equivalent circuit, in which  $R_s$ ,  $R_{ct}$ , and CPE are solution resistance, charge-transfer resistance between catalyst and electrolyte, and constant-phase element, respectively. (g) Chronopotentiometry responses of NCoFO/CC-60, CoFO/CC, Pt/C, and  $\text{RuO}_2$  for HER and OER at a constant current density of  $10 \text{ mA cm}^{-2}$ .

resolution F 1s XPS spectra of NCoFO/CC-60 are depicted in Figure 3c. No significant shifts in the peak positions of the F 1s spectrum were observed, indicating no apparent modulation of electron density in the neighboring fluorine atoms.<sup>12,26,31</sup> In Figure 3d, the O 1s peak displayed a broad fitted peak at 531.9 eV, which can be attributed to Co–O bonds related to metal–oxygen interactions<sup>12,26</sup> (Figure 3d). The deconvoluted peak at 532.9 eV corresponded to surface-dominated oxygen species, indicating the successful formation of cobalt-fluoride-oxide complexes.<sup>12</sup>

**2.3. HER and OER Electrocatalysis.** The HER catalytic performances of NCoFO/CC-60, CoFO/CC,  $\text{Co}_3\text{O}_4/\text{CC}$ , and CC were evaluated using a three-electrode setup with commercial Pt/C catalysts for comparison. Figure 4a illustrates the linear sweep voltammetry (LSV) curves obtained at a sweep rate of  $10 \text{ mV s}^{-1}$  in a  $\text{N}_2$ -saturated 1.0 M KOH solution. Notably, NCoFO/CC-60 achieved an overpotential of 203 mV to attain a current density of  $10 \text{ mA cm}^{-2}$ , which was significantly lower compared to those of CoFO/CC (281 mV),  $\text{Co}_3\text{O}_4/\text{CC}$  (303 mV), and CC (521 mV). In comparison, the state-of-the-art precious-metal-based Pt/C catalyst exhibited an overpotential of 63 mV at the same current density of  $10 \text{ mA cm}^{-2}$ . This result clearly indicates that the incorporation of nitrogen greatly enhanced the HER activity of CoFO/CC. Furthermore, NCoFO/CC-60 also demonstrated an ultralow overpotential of 298 mV to achieve a

current density of  $100 \text{ mA cm}^{-2}$ , in contrast to those of CoFO/CC (391 mV) and  $\text{Co}_3\text{O}_4/\text{CC}$  (425 mV). This highlights the desirable HER performance of NCoFO/CC-60 even at high current densities. The HER performance of NCoFO/CC-60 surpassed that of most reported non-noble-metal-based HER electrocatalysts under the same conditions (Table S2). Tafel slopes were examined to further assess the HER activity. As depicted in Figure 4b, the Tafel slope of NCoFO/CC-60 was measured to be  $66 \text{ mV dec}^{-1}$ , significantly lower than those of CoFO/CC ( $91 \text{ mV dec}^{-1}$ ) and  $\text{Co}_3\text{O}_4/\text{CC}$  ( $111 \text{ mV dec}^{-1}$ ), and even comparable to that of Pt/C ( $55 \text{ mV dec}^{-1}$ ). Additionally, the time-dependent activities of NCoFO/CC due to plasma treatment were investigated, as shown in Figure S9. The optimum HER catalytic performance was achieved at a plasma treatment time of 60 s. For comparison, we also performed the HER performance test on a  $\text{Co}(\text{OH})_2$  sample with a plasma treatment time of 60 s ( $\text{N-Co}(\text{OH})_2/\text{CC-60}$ ). The results revealed that NCoFO/CC-60 still exhibited higher catalytic activity than  $\text{N}_2$  plasma-activated  $\text{N-Co}(\text{OH})_2/\text{CC-60}$  (Figure S10). The findings indicate that the incorporation of fluorine into the lattice plays a crucial role in enhancing the HER activity during the subsequent plasma treatment. Moreover, NCoFO/CC-60 demonstrated a significantly higher double-layer capacitance ( $C_{dl}$ ) of  $5.57 \text{ mF cm}^{-2}$  than that of CoFO/CC ( $4.33 \text{ mF cm}^{-2}$ ), indicating more abundant active sites after N doping (Figure S11).<sup>6</sup> Therefore,

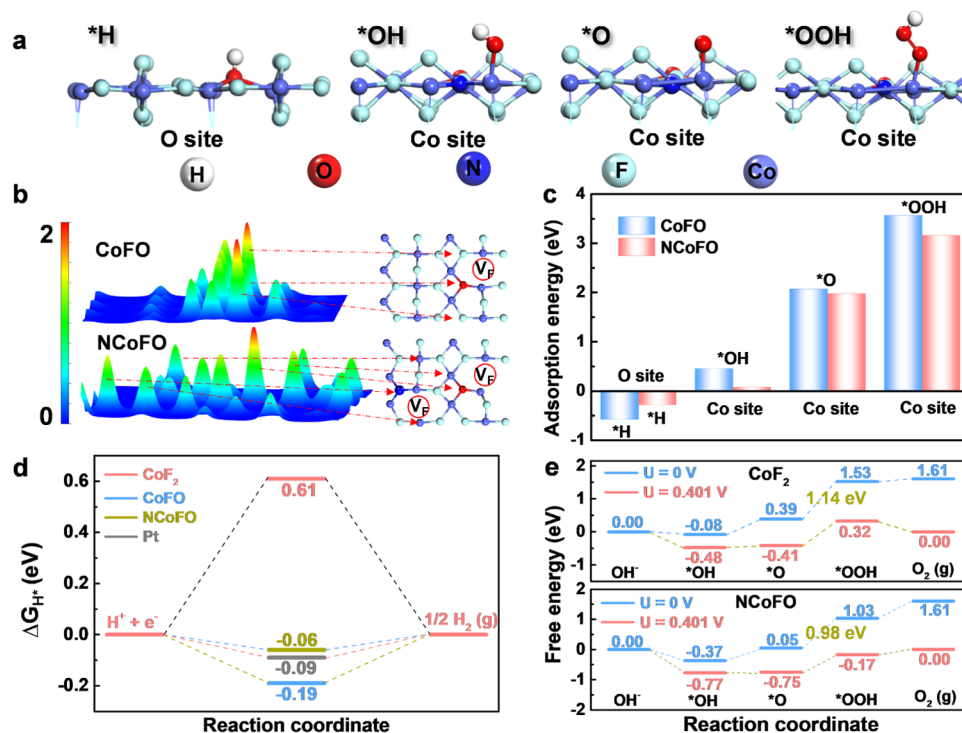


**Figure 5.** (a) Schematic of \*H adsorbed on the O active site of NCoFO for HER and \*OH, \*O, and \*OOH intermediates in the Co active sites of NCoFO for OER. The symmetric parts of the optimized slabs at the bottom are excluded for clarity. (b) Electron density difference plot of the CoFO and NCoFO. Electron density increased with the color change from blue to red. (c) Adsorption energies (eV) for \*OH, \*O, \*OOH, and O<sub>2</sub>(g) adsorbed on the Co active sites. (d) Calculated adsorption free energy of hydrogen on different active sites of CoF<sub>2</sub>, CoFO, and NCoFO, respectively. (e) Free-energy diagram of OER at different voltages (indicated by different colors) on the Co active sites of CoFO (110) and NCoFO (110) in the alkaline electrolyte.

it can be concluded that only the codoping of fluorine and nitrogen in Co(OH)<sub>2</sub> leads to an improvement in the HER performance.

The electrocatalytic activities for the OER of NCoFO/CC-60, CoFO/CC, Co<sub>3</sub>O<sub>4</sub>/CC, CC, and RuO<sub>2</sub> were evaluated in a 1.0 M KOH solution. The LSV curves (Figure 4c) revealed that the NCoFO/CC-60 catalyst exhibited the highest OER performance, requiring an overpotential of only 230 mV to achieve a current density of 10 mA cm<sup>-2</sup>. This overpotential was significantly lower compared with CoFO/CC (340 mV) and Co<sub>3</sub>O<sub>4</sub>/CC (358 mV) catalysts. Furthermore, NCoFO/CC-60 demonstrated an exceptionally low overpotential of 300 mV at a current density of 100 mA cm<sup>-2</sup>, even outperforming RuO<sub>2</sub> (320 mV). These results highlight the remarkable catalytic activity of NCoFO/CC-60 toward the OER, even at high current densities. Additionally, when compared with other nonprecious metal-based electrocatalysts reported in the literature (Table S3), the measured overpotential of NCoFO/CC-60 was also smaller, further emphasizing its superior performance. Furthermore, NCoFO/CC-60 exhibited the lowest Tafel slope of 62 mV dec<sup>-1</sup> compared to those of CoFO/CC (75 mV dec<sup>-1</sup>), Co<sub>3</sub>O<sub>4</sub>/CC (109 mV dec<sup>-1</sup>), and RuO<sub>2</sub> (88 mV dec<sup>-1</sup>), demonstrating its exceptional kinetic activity for the OER (Figure 4d). However, it was observed that the OER performance decreased with prolonged plasma-treatment times of 30 or 90 s (Figure S12), indicating that the optimal plasma-treatment time was 60 s. To gain insights into the interfacial electron-transfer dynamics during the OER, electrochemical impedance spectroscopy (EIS) was conducted. The equivalent circuit (inset of Figure 4f) comprised an electrolyte resistance (*R*<sub>s</sub>) in series with a parallel combination

of a constant-phase element and a charge-transfer resistance (*R*<sub>ct</sub>). The Nyquist plot revealed a smaller *R*<sub>s</sub> of NCoFO/CC-60 (2.0 Ω) compared to that of CoFO/CC (2.3 Ω), indicating that NCoFO/CC-60 had a low internal and interfacial resistance between its surface and the electrolyte. Furthermore, NCoFO/CC-60 demonstrated a smaller charge-transfer resistance (*R*<sub>ct</sub>) of 5.0 Ω compared to CoFO/CC (11.7 Ω), indicating faster mass-transfer kinetics during OER.<sup>7</sup> While some catalysts may initially demonstrate high activity, they often experience a rapid decay in performance due to surface or bulk reconstruction.<sup>32</sup> Remarkably, NCoFO/CC-60 demonstrated a negligible change in the HER and the OER after 10 000 s of chronopotentiometry testing, surpassing the tested samples (Figure 4g). In contrast, Pt/C/CC and RuO<sub>2</sub> displayed a noticeable decrease in activity over the same testing period, highlighting the exceptional durability of NCoFO/CC-60 in both the HER and the OER.

#### 2.4. Mechanistic Study on HER and OER of Materials.

In order to elucidate the enhanced activity of plasma-treated NCoFO-CC samples for the HER and the OER, density functional theory (DFT) calculations were conducted to investigate the effects of nitrogen (N) doping on the atomic and electronic structures of CoFO. Considering the experimental results obtained from XRD and HRTEM, the high-index (110) plane of the materials was selected as the active surface. Adsorption sites of \*H or \*OH, \*O, and \*OOH species on the pristine CoF<sub>2</sub>, CoFO, and NCoFO surface (including N, Co, O, or F atom sites) were considered, consistent with the experimental stoichiometry (Figure 5a). The top view structures of CoF<sub>2</sub>, CoFO, and NCoFO (110) with bond lengths are presented in Figure S13. Notably, the

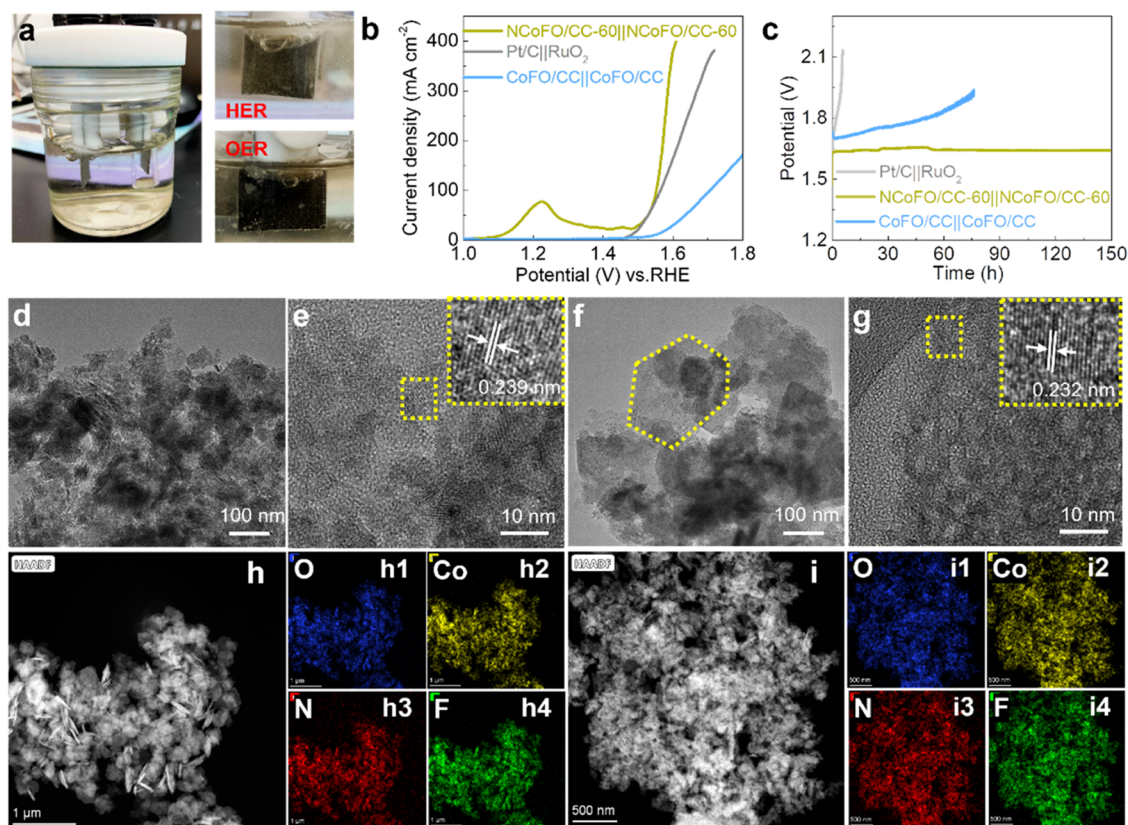


**Figure 6.** (a) Optical photos of the coupled system: O<sub>2</sub> evolution (left), electrolysis (middle), and H<sub>2</sub> evolution (right). (b) LSV curves of the NCoFO/CC-60||NCoFO/CC-60, CoFO/CC||CoFO/CC, and Pt/C||RuO<sub>2</sub> electrodes in 1.0 M KOH solution at 10 mV s<sup>-1</sup> with IR compensation in a two-electrode system. (c) Chronopotentiometric curves of water electrolysis for NCoFO/CC-60||NCoFO/CC-60, CoFO/CC||CoFO/CC, and Pt/C||RuO<sub>2</sub> electrodes in 1.0 M KOH solution. (d) TEM image and (e) HRTEM image of NCoFO/CC-60 after HER test. (f) TEM image and (g) HRTEM image of NCoFO/CC-60 after OER test. SEM images with the corresponding EDX mapping of various elements in the porous NCoFO/CC-60 nanosheet after (h) HER test and (i) OER test.

observed Co–F bond length (1.934 to 2.122 Å) in NCoFO was greater than that in pristine CoF<sub>2</sub> (1.972 to 2.050 Å) and CoFO (1.972 to 2.099 Å), which can be attributed to the weaker electronegativity of the N atom compared to that of the F atom. Therefore, the substantial N incorporation effectively regulates the electronic structure and adsorption energy of active sites, subsequently weakening the ionicity in Co–F bonds. In order to elucidate the relationship between N dopants and the electron densities of active sites, we have provided electron density difference maps of CoFO and NCoFO in Figure S5b. The introduction of N dopants led to the formation of V<sub>F</sub> sites due to electronic reconstruction within the system. It is evident from the maps that in CoFO, the majority of electrons were localized on F atoms near oxygen atoms, as F atoms have higher electronegativity (3.98 Pauling scale) compared to that of the electrons on the O atoms (3.44 Pauling scale). However, in NCoFO, the electrons of the F atoms tended to migrate toward nitrogen atoms and Co atoms, resulting in the formation of strong Co=N bonds. This finding suggested that N dopants led to F vacancies and greatly optimized the electronic structure. Furthermore, the Bader charges of CoFO and NCoFO were examined to investigate the charge density of atoms after N doping, and the results are shown in Figure S14. After N doping, the number of electrons lost by Co atoms near N atoms decreases, indicating a decrease in the valence state of Co, which is consistent with the XPS results (Figure 3).

To gain a deeper understanding of the impact of incorporated N atoms on the HER, the proton adsorption energy and energy profiles were investigated, as presented in Figures S5c,d and S15. HER typically involves two steps in alkaline conditions: (i) the generation of \*H from adsorbed H<sub>2</sub>O (\*H<sub>2</sub>O) on the material's surface and (ii) the combination of another H from the HO–H bond with \*H to form adsorbed H<sub>2</sub> (\*H<sub>2</sub>), followed by the desorption of the H<sub>2</sub> molecule from the catalyst surface. The crucial factor enabling favorable HER is typically the appropriate binding energy of atomic hydrogen on the material, specifically the adsorption of H atoms on the \* and \*H sites. To assess this, we calculated the adsorption energies of \*H in CoF<sub>2</sub>, CoFO, and NCoFO, considering different active sites, as depicted in Figure S15d. Considering the distinct coordination environments of each element on the surface, we identified the top F atom, surface F atom, and surface Co atom as the active sites for pristine CoF<sub>2</sub>. After the O element through doping, the doped O atom was included as an additional active site for CoFO (Figure S15e). Similarly, for NCoFO, the surface N atom was chosen as an additional active site (Figure S15f). Notably, the calculated lower adsorption energies of \*H at the O sites in NCoFO (–0.3 eV) compared to CoFO (–0.6 eV) indicated more favorable HER occurrences at the neighboring O sites within the NCoFO slab (Figure 5c). To gain further insights into the improved HER activity, the Gibbs free energy of the adsorbed \*H (ΔG<sub>\*H</sub>) on the catalyst surface was

evaluated. As illustrated in Figure 5d, the CoFO (110) surface exhibited a lower  $\Delta G_{*H}$  of  $-0.19$  eV on the O sites, indicating a more favorable adsorption of H. Interestingly, after N incorporation,  $\Delta G_{*H}$  decreased to  $-0.06$  eV on the O sites, which was closer to that of Pt (111) ( $-0.09$  eV). This observation suggests the superior catalytic performance of NCoFO on the O-top site, which is attributed to the surface electronic modulation resulting from N doping.

The adsorption behaviors of key intermediates ( $*OH$ ,  $*O$ , and  $*OOH$ ) during the OER were investigated on the surface, revealing that the Co sites were stable for the adsorption of the OER intermediates. Subsequently, we examined various levels of N doping in NCoFO, and the detailed descriptions are provided in Figure S16. To further disclose the nature of the difference in the level of the OER activity among  $CoF_2$ , CoFO, and NCoFO, we calculated the Gibbs free energy profiles. As depicted in Figures 5e and S16, the rate-determining step for the OER on the Co centers of  $CoF_2$ , CoFO, and NCoFO was the conversion of  $*O$  to  $*OOH$ . However, NCoFO exhibited a significantly enhanced activity with a substantially lower overpotential of  $0.83$  V, compared to  $1.14$  V for pristine  $CoF_2$  (Figure S17) and  $1.03$  V for CoFO. These results clearly indicate that N incorporation effectively reduces the overpotential for the OER and promotes the catalytic activity.

**2.5. Performance on Water Splitting of Materials and Stability Test.** Motivated by the enhanced HER and OER activities, we conducted alkaline water splitting tests using CoFO/CC and NCoFO/CC-60 electrocatalysts as bifunctional electrodes. For comparison, commercially available Pt/C and  $RuO_2$  (Pt/C|| $RuO_2$ ) were employed as the cathode and anode electrodes, respectively. As the applied potential increased, gas bubble formation ( $H_2$  and  $O_2$ ) was observed at the electrodes (Figure 6a). The LSV curves of NCoFO/CC-60||NCoFO/CC-60 demonstrated that an exceptionally low overall voltage of  $1.48$  V was required to achieve a current density of  $10$  mA  $cm^{-2}$  (Figure 6b), surpassing the performance of Pt/C+ $RuO_2$  ( $1.50$  V) and CoFO/CC ( $1.55$  V) (Table S4). To evaluate the long-term stability of the symmetrical cell utilizing NCoFO/CC-60 electrodes, we conducted continuous water splitting experiments, as depicted in Figure 6c. Following continuous operation at  $10$  mA  $cm^{-2}$  for  $150$  h, the potential of the NCoFO/CC-60||NCoFO/CC-60 assembled electrolytic cell demonstrated a minimal increase, from  $1.67$  V initially to  $1.69$  V around the  $54$  h mark, after which it remained stable. Notably, the NCoFO/CC-60||NCoFO/CC-60 configuration exhibited a slight rise in the OER overpotential, approximately  $1.69\%$ , throughout the  $150$  h operation period (see Figure S18). In contrast, the CoFO/CC||CoFO/CC and Pt/C|| $RuO_2$  electrolytic cells exhibited a notable increase in the potential over a short period of time. This exceptional electrocatalytic activity and durability observed in NCoFO/CC-60 highlight its potential as a valuable alternative for HER and OER electrocatalysis, surpassing those of commercial Pt/C and  $RuO_2$  counterparts. This suggests that NCoFO/CC-60 could serve as a cost-effective and energy-efficient alternative for water splitting applications.

The stability of a catalyst's structure is typically correlated with its operational durability, while structural reconstructions can impact the catalytic activity positively or negatively. To investigate the exceptional catalytic durability of NCoFO/CC-60, XPS spectra were obtained after HER and OER operations (Figures S18 and S19, respectively). The survey spectra

revealed that the tested sample (Figure 6d–i and Table S4) maintained the presence of Co, F, O, and N elements even after the durability test as HER or OER electrocatalysts. However, a significant change in the atomic percentage of F and O was observed in the energy spectrum following the long-term test. Significantly, the atomic percentage of F exhibited a substantial decrease from  $8.79$  to  $1.73$  and  $2.07\%$  after the HER and OER tests, respectively. This suggests that significant F leaching occurred during HER and OER, leading to surface reconstruction.<sup>33</sup> Conversely, the atomic percentage of O increased from  $23.72$  to  $35.01$  and  $43.19\%$ , respectively. The XRD patterns of the tested electrodes indicated that NCoFO/CC-60 underwent partial conversion into  $Co(OH)_2$  and  $CoOOH$  after HER and OER operations (Figure S19). However, the N 1s spectrum revealed no significant change in its atomic percentage after the prolonged HER and OER tests. Additionally, the atomic percentage of the Co 2p spectrum slightly increased following the prolonged HER and OER tests.

The SEM images were used to examine the morphology of the NCoFO/CC-60 electrocatalysts after an extended test period. Figures S20 and S21 illustrate the observed changes. After the HER stability test, the original hierarchical porous nanosheets underwent a smooth transformation, resulting in thick nanoplates (Figure S20). Conversely, after the OER stability test, the morphology transformed into porous nanostructures (Figure S21). To gain further insights into the morphology and structural reconstruction of the electrocatalyst following the HER and OER performance tests, TEM and HRTEM characterizations were conducted. The electrocatalyst exhibited a nonuniform nanostructure after the OER test. Additionally, a lattice fringe measuring  $0.232$  nm was observed, corresponding to the (012) diffraction plane of  $CoOOH$ . This observation suggests that there was a bulk reconstruction in response to the changes in composition and morphology, which likely contributed to the preservation of the catalytic activity. Following the HER test, the electrocatalyst exhibited a hexagonal nanosheet morphology, as depicted in Figure 6f,g. The corresponding d-space was measured to be  $0.239$  nm, aligned with the (101) diffraction plane of  $Co(OH)_2$ . Furthermore, EDS mapping analysis revealed the presence of Co, F, O, and N elements in the material, consistent with the findings from XPS characterization. These observations indicate that the prolonged test induced a phase change in the material, leading to a modified morphology while preserving its elemental composition.

To gain further insights into the structure–activity relationship of the electrocatalyst concerning its performance in the HER and OER tests, we conducted additional analysis by calculating Bader charges using DFT. This approach allowed us to qualitatively examine the changes in the valence states of Co atoms in  $Co(OH)_2$  and  $CoOOH$  (Figure S22). The results revealed that the Co atoms in  $Co(OH)_2$  exhibited a low-charge state with only  $0.68$   $e^-$  ( $Co^{2+}$ ), while the valence state of the Co atoms in  $CoOOH$  increased, showing an average positive charge of  $1.28$   $e^-$  ( $Co^{3+}$ ). Notably, a higher valence state of Co atoms in  $CoOOH$  was observed after the OER test. This increase in the valence state may be attributed to the oxidation of  $OH^-$  to form  $O_2$ , facilitated by the higher electronegativity of the O atom, which tends to gain electrons. Upon the phase transformation to  $CoOOH$ , there was a partial transfer of electrons from the Co sites to the adsorbed intermediates through the bridging  $O^{2-}$  ions. This electron transfer increased

the electron density of the Co sites and resulted in a partial reduction in the valence states of Co. As a result, the bonding strength between the Co sites and oxygen-containing intermediates was subtly optimized, facilitating the release of O<sub>2</sub> from the Co site.<sup>34</sup> It is important to note that the HER involves the acquisition of electrons, and the HER performance is primarily determined by the  $\Delta G_{*H}$  value. In our HER results, we observed that \*H preferentially adsorbed onto the O-site of both CoFO and NCoFO catalysts, indicating favorable  $\Delta G_{*H}$  values (−0.19 eV for CoFO and −0.06 eV for NCoFO; Figure S15) close to zero, suggesting high catalytic activity. However, after prolonged HER, the original NCoFO phase underwent a transformation into Co(OH)<sub>2</sub>, where the saturated O atoms were uniformly covered by \*H, causing the active site to shift from the original O-site to the Co-site. The calculated  $\Delta G$  of the Co site in Co(OH)<sub>2</sub> was found to be −0.24 eV (Table S6), which was still superior to those of the other active sites (Co, N, and F) in NCoFO (Figure S16c). DFT results revealed the significant change in  $\Delta G_{*H}$  value of the Co site in the transformed Co(OH)<sub>2</sub> phase compared to the original NCoFO phase. This indicates that the phase transformation from NCoFO to Co(OH)<sub>2</sub> enhances the efficiency and stability of the hydrogen evolution. The change in the valence state of Co from Co<sup>3+</sup> sites to Co<sup>2+</sup> is attributed to hydrogen adsorption at the Co site, leading to the reduction of Co<sup>3+</sup> to Co<sup>2+</sup> and stronger chemical adsorption of \*H.<sup>35</sup> Consequently, the low-charge-state Co atom in the transformed Co(OH)<sub>2</sub> phase is favorable for the HER reduction process, promoting H<sub>2</sub> gas production.

### 3. CONCLUSIONS

A novel approach involving N<sub>2</sub> plasma treatment was proposed to weaken the high ionicity in Co–F bonds within CoFO materials, leading to remarkable improvements in HER and OER performance and enhanced stability in alkaline solutions. The N-doped NCoFO/CC-60 electrocatalyst, with a N-doping level of 3.04 atom %, exhibited impressive HER and OER activities in a 1.0 M KOH solution, achieving overpotentials of 203 and 230 mV, respectively, at a current density of 10 mA cm<sup>−2</sup>. Notably, an ultralow potential of 1.48 V was recorded for NCoFO/CC-60||NCoFO/CC-60 electrodes during 150 h of continuous operation for overall water splitting in a 1.0 M KOH solution, surpassing the performance of a Pt/C||RuO<sub>2</sub> electrode that achieved 10 mA cm<sup>−2</sup> with a potential of 1.50 V but only for 5.6 h. In-depth DFT calculations revealed that the introduction of N atoms triggered coordinated adjustments in the electronic structure of NCoFO, enhancing the electron delocalization capacity of Co atoms, leading to improved electrical conductivity, and optimizing the free energy of \*H desorption on O atoms. Furthermore, the calculations also demonstrated the electronic state changes of the Co active sites during bulk reconstruction, which contribute to maintaining the high catalytic activities for both the HER and the OER. This study highlights the effectiveness of the N<sub>2</sub> plasma approach for introducing N dopants at the atomic level and modulating the electronic structure of metal-oxide electrodes to enhance their catalytic properties.

### ■ ASSOCIATED CONTENT

#### SI Supporting Information

The Supporting Information is available free of charge at <https://pubs.acs.org/doi/10.1021/acscatal.4c00294>.

Experimental section; computational methods; XRD pattern of Co(OH)<sub>2</sub>/CC; SEM images of Co(OH)<sub>2</sub>/CC (a, b), and CoFO/CC (c, d); summary of recent progress on HER reactivity of transition metal compounds; comparison of overall water splitting performance of recently reported transition metal-based bifunctional electrocatalysts and related references (PDF)

### ■ AUTHOR INFORMATION

#### Corresponding Authors

**Kwan San Hui** – School of Engineering, Faculty of Science, University of East Anglia, Norwich NR4 7TJ, U.K.; [orcid.org/0000-0001-7089-7587](https://orcid.org/0000-0001-7089-7587); Email: [k.hui@uea.ac.uk](mailto:k.hui@uea.ac.uk)

**Young-Rae Cho** – School of Materials Science and Engineering, Pusan National University, Busan 609-735, Republic of Korea; [orcid.org/0000-0003-0591-1463](https://orcid.org/0000-0003-0591-1463); Email: [yescho@pusan.ac.kr](mailto:yescho@pusan.ac.kr)

**Kwun Nam Hui** – Joint Key Laboratory of the Ministry of Education, Institute of Applied Physics and Materials Engineering, University of Macau, Avenida da Universidade, Taipa, Macau SAR 999078, China; [orcid.org/0000-0002-3008-8571](https://orcid.org/0000-0002-3008-8571); Email: [bizhui@um.edu.mo](mailto:bizhui@um.edu.mo)

#### Authors

**Shuo Wang** – Joint Key Laboratory of the Ministry of Education, Institute of Applied Physics and Materials Engineering, University of Macau, Avenida da Universidade, Taipa, Macau SAR 999078, China

**Cheng-Zong Yuan** – Joint Key Laboratory of the Ministry of Education, Institute of Applied Physics and Materials Engineering, University of Macau, Avenida da Universidade, Taipa, Macau SAR 999078, China; Jiangxi Province Key Laboratory of Cleaner Production of Rare Earths, Ganjiang Innovation Academy, Chinese Academy of Sciences, Ganzhou 341119, China; [orcid.org/0000-0002-4767-8957](https://orcid.org/0000-0002-4767-8957)

**Yunshan Zheng** – Joint Key Laboratory of the Ministry of Education, Institute of Applied Physics and Materials Engineering, University of Macau, Avenida da Universidade, Taipa, Macau SAR 999078, China

**Yao Kang** – Joint Key Laboratory of the Ministry of Education, Institute of Applied Physics and Materials Engineering, University of Macau, Avenida da Universidade, Taipa, Macau SAR 999078, China

**Kaixi Wang** – Joint Key Laboratory of the Ministry of Education, Institute of Applied Physics and Materials Engineering, University of Macau, Avenida da Universidade, Taipa, Macau SAR 999078, China

**Haixing Gao** – Joint Key Laboratory of the Ministry of Education, Institute of Applied Physics and Materials Engineering, University of Macau, Avenida da Universidade, Taipa, Macau SAR 999078, China

**Duc Anh Dinh** – NTT Hi-Tech Institute, Nguyen Tat Thanh University, Ho Chi Minh City 700000, Vietnam

Complete contact information is available at: <https://pubs.acs.org/doi/10.1021/acscatal.4c00294>

#### Author Contributions

#S.W., C.-Z.Y., and Y.Z. contributed equally to this work.

#### Notes

The authors declare no competing financial interest.

## ACKNOWLEDGMENTS

This work was financially supported by the Science and Technology Development Fund, Macau SAR (File Nos. 0046/2019/AFJ, 0041/2019/A1, 0007/2021/AGJ, 0070/2023/AFJ), the University of Macau (File Nos. MYRG2018-00192-IAPME, MYRG2020-00187-IAPME, MYRG2022-00223-IAPME), the Natural Science Foundation and Overseas Talent Projects of Jiangxi Province (20232BAB214025, 20232BCJ25044), the National Research Foundation of Korea (NRF) grant funded by the Korea government (MSIT) (No. RS-2023-00276980), and the UEA funding. The DFT calculations are performed at High-Performance Computing Cluster (HPCC) of Information and Communication Technology Office (ICTO) at the University of Macau.

## REFERENCES

- (1) Chu, S.; Majumdar, A. Opportunities and challenges for a sustainable energy future. *Nature* **2012**, *488* (7411), 294–303. Stamenkovic, V. R.; Strmcnik, D.; Lopes, P. P.; Markovic, N. M. Energy and fuels from electrochemical interfaces. *Nat. Mater.* **2017**, *16* (1), 57–69. Roger, I.; Shipman, M. A.; Symes, M. D. Earth-abundant catalysts for electrochemical and photoelectrochemical water splitting. *Nat. Rev. Chem.* **2017**, *1* (1), No. 0003, DOI: 10.1038/s41570-016-0003.
- (2) Ye, S.; Luo, F.; Zhang, Q.; Zhang, P.; Xu, T.; Wang, Q.; He, D.; Guo, L.; Zhang, Y.; He, C.; Ouyang, X.; Gu, M.; Liu, J.; Sun, X. Highly stable single Pt atomic sites anchored on aniline-stacked graphene for hydrogen evolution reaction. *Energy Environ. Sci.* **2019**, *12* (3), 1000–1007. Yeo, B. S. Oxygen evolution by stabilized single Ru atoms. *Nat. Catal.* **2019**, *2* (4), 284–285.
- (3) Forgie, R.; Bugosh, G.; Neyerlin, K. C.; Liu, Z.; Strasser, P. Bimetallic Ru Electrocatalysts for the OER and Electrolytic Water Splitting in Acidic Media. *Electrochem. Solid-State Lett.* **2010**, *13* (4), No. B36, DOI: 10.1149/1.3290735. Lu, J.; Tang, Z.; Luo, L.; Yin, S.; Kang Shen, P.; Tsiakaras, P. Worm-like S-doped RhNi alloys as highly efficient electrocatalysts for hydrogen evolution reaction. *Appl. Catal., B* **2019**, *255*, No. 117737, DOI: 10.1016/j.apcatb.2019.05.039. Sun, H.; Yan, Z.; Liu, F.; Xu, W.; Cheng, F.; Chen, J. Self-Supported Transition-Metal-Based Electrocatalysts for Hydrogen and Oxygen Evolution. *Adv. Mater.* **2020**, *32* (3), No. 1806326, DOI: 10.1002/adma.201806326. Yuan, C.-Z.; Hui, K. S.; Yin, H.; Zhu, S.; Zhang, J.; Wu, X.-L.; Hong, X.; Zhou, W.; Fan, X.; Bin, F.; Chen, F.; Hui, K. N. Regulating Intrinsic Electronic Structures of Transition-Metal-Based Catalysts and the Potential Applications for Electrocatalytic Water Splitting. *ACS Mater. Lett.* **2021**, *3* (6), 752–780.
- (4) Morales, D. M.; Kazakova, M. A.; Dieckhöfer, S.; Selyutin, A. G.; Golubtsov, G. V.; Schuhmann, W.; Masa, J. Trimetallic Mn-Fe-Ni Oxide Nanoparticles Supported on Multi-Walled Carbon Nanotubes as High-Performance Bifunctional ORR/OER Electrocatalyst in Alkaline Media. *Adv. Funct. Mater.* **2020**, *30* (6), No. 1905992. Li, J.; Chu, D.; Dong, H.; Baker, D. R.; Jiang, R. Boosted Oxygen Evolution Reactivity by Igniting Double Exchange Interaction in Spinell Oxides. *J. Am. Chem. Soc.* **2020**, *142* (1), 50–54. Browne, M. P.; Sofer, Z.; Pumera, M. Layered and two dimensional metal oxides for electrochemical energy conversion. *Energy Environ. Sci.* **2019**, *12* (1), 41–58.
- (5) Gao, Y.; Han, Z.; Cao, Y.; Sun, X.; Zhuang, G.; Deng, S.; Zhong, X.; Wei, Z.; Wang, J. A theoretical study of electrocatalytic ammonia synthesis on single metal atom/Mxene. *Chin. J. Catal.* **2019**, *40* (2), 152–159.
- (6) Cai, J.; Song, Y.; Zang, Y.; Niu, S.; Wu, Y.; Xie, Y.; Zheng, X.; Liu, Y.; Lin, Y.; Liu, X.; Wang, G.; Qian, Y. N-induced lattice contraction generally boosts the hydrogen evolution catalysis of P-rich metal phosphides. *Sci. Adv.* **2020**, *6* (1), No. eaaw8113, DOI: 10.1126/sciadv.aaw8113.
- (7) Wu, Y.; Tao, X.; Qing, Y.; Xu, H.; Yang, F.; Luo, S.; Tian, C.; Liu, M.; Lu, X. Cr-Doped FeNi–P Nanoparticles Encapsulated into N-Doped Carbon Nanotube as a Robust Bifunctional Catalyst for Efficient Overall Water Splitting. *Adv. Mater.* **2019**, *31* (15), No. 1900178.
- (8) Dutta, S.; Indra, A.; Feng, Y.; Han, H.; Song, T. Promoting electrocatalytic overall water splitting with nanohybrid of transition metal nitride-oxynitride. *Appl. Catal., B* **2019**, *241*, 521–527. Wu, M.; Zhang, G.; Qiao, J.; Chen, N.; Chen, W.; Sun, S. Ultra-long life rechargeable zinc-air battery based on high-performance trimetallic nitride and NCNT hybrid bifunctional electrocatalysts. *Nano Energy* **2019**, *61*, 86–95. Lv, M.; Zhou, Y.; Abolaji, R. S.; Shen, H.; Chuanxi, W.; Song, W.; Thomas, T.; Yang, M.; Wang, J. Gold (Au) nanocluster decorated Nickel nitride as stable electrocatalyst for oxygen evolution reaction in alkaline solution. *ChemElectroChem* **2019**, *6*, 5744–5749, DOI: 10.1002/celec.201901439. Wang, K.; Guo, Y.; Chen, Z.; Wu, D.; Zhang, S.; Yang, B.; Zhang, J. Regulating electronic structure of two-dimensional porous Ni/Ni<sub>3</sub>N nanosheets architecture by Co atomic incorporation boosts alkaline water splitting. *InfoMat* **2022**, *4* (6), No. e12251, DOI: 10.1002/inf2.12251.
- (9) Wang, K.; Wang, S.; Hui, K. S.; Gao, H.; Dinh, D. A.; Yuan, C.; Zha, C.; Shao, Z.; Tang, Z.; Hui, K. N. Synergistically boosting the elementary reactions over multiheterogeneous ordered macroporous Mo<sub>2</sub>C/NC-Ru for highly efficient alkaline hydrogen evolution. *Carbon Energy* **2022**, *4*, 856–866, DOI: 10.1002/cey2.188. Suliman, M. H.; Adam, A.; Li, L.; Tian, Z.; Siddiqui, M. N.; Yamani, Z. H.; Qamar, M. FeP/MoS<sub>2</sub> Enriched with Dense Catalytic Sites and High Electrical Conductivity for the Hydrogen Evolution Reaction. *ACS Sustainable Chem. Eng.* **2019**, *7* (21), 17671–17681. Cheng, Y.; Guo, H.; Yuan, P.; Li, X.; Zheng, L.; Song, R. Self-supported bifunctional electrocatalysts with Ni nanoparticles encapsulated in vertical N-doped carbon nanotube for efficient overall water splitting. *Chem. Eng. J.* **2021**, *413*, No. 127531, DOI: 10.1016/j.cej.2020.127531.
- (10) Yang, H.; Chen, Z.; Guo, P.; Fei, B.; Wu, R. B-doping-induced amorphization of LDH for large-current-density hydrogen evolution reaction. *Appl. Catal., B* **2020**, *261*, No. 118240. Tang, Y.; Liu, Q.; Dong, L.; Wu, H. B.; Yu, X.-Y. Activating the hydrogen evolution and overall water splitting performance of NiFe LDH by cation doping and plasma reduction. *Appl. Catal., B* **2020**, *266*, No. 118627, DOI: 10.1016/j.apcatb.2020.118627.
- (11) Zhang, N.; Li, X.; Ye, H.; Chen, S.; Ju, H.; Liu, D.; Lin, Y.; Ye, W.; Wang, C.; Xu, Q.; Zhu, J.; Song, L.; Jiang, J.; Xiong, Y. Oxide Defect Engineering Enables to Couple Solar Energy into Oxygen Activation. *J. Am. Chem. Soc.* **2016**, *138* (28), 8928–8935.
- (12) Han, H.; Woo, J.; Hong, Y.-R.; Chung, Y.-C.; Mhin, S. Polarized Electronic Configuration in Transition Metal–Fluoride Oxide Hollow Nanoprism for Highly Efficient and Robust Water Splitting. *ACS Appl. Energy Mater.* **2019**, *2* (6), 3999–4007.
- (13) Laursen, A. B.; Varela, A. S.; Dionigi, F.; Fanchiu, H.; Miller, C.; Trinhammer, O. L.; Rossmeisl, J.; Dahl, S. Electrochemical hydrogen evolution: sabatier's principle and the volcano plot. *J. Chem. Educ.* **2012**, *89* (12), 1595–1599. Medford, A. J.; Vojvodic, A.; Hummelshøj, J. S.; Voss, J.; Abild-Pedersen, F.; Studt, F.; Bligaard, T.; Nilsson, A.; Nørskov, J. K. From the Sabatier principle to a predictive theory of transition-metal heterogeneous catalysis. *J. Catal.* **2015**, *328*, 36–42.
- (14) Huang, K.; Zhao, Z.; Du, H.; Du, P.; Wang, H.; Wang, R.; Lin, S.; Wei, H.; Long, Y.; Lei, M.; Guo, W.; Wu, H. Rapid thermal annealing toward high-quality 2D cobalt fluoride oxide as an advanced oxygen evolution electrocatalyst. *ACS Sustainable Chem. Eng.* **2020**, *8* (18), 6905–6913.
- (15) Xu, L.; Wang, Z.; Wang, J.; Xiao, Z.; Huang, X.; Liu, Z.; Wang, S. N-doped nanoporous Co<sub>3</sub>O<sub>4</sub> nanosheets with oxygen vacancies as oxygen evolving electrocatalysts. *Nanotechnology* **2017**, *28*, No. 165402.
- (16) Yu, M.; Wang, Z.; Hou, C.; Wang, Z.; Liang, C.; Zhao, C.; Tong, Y.; Lu, X.; Yang, S. Nitrogen-Doped Co<sub>3</sub>O<sub>4</sub> Mesoporous Nanowire Arrays as an Additive-Free Air-Cathode for Flexible Solid-State Zinc–Air Batteries. *Adv. Mater.* **2017**, *29* (15), No. 1602868.

- (17) Lin, J.; Yan, Y.; Xu, T.; Qu, C.; Li, J.; Cao, J.; Feng, J.; Qi, J. S. doped NiCo<sub>2</sub>O<sub>4</sub> nanosheet arrays by Ar plasma: An efficient and bifunctional electrode for overall water splitting. *J. Colloid Interface Sci.* **2020**, *560*, 34–39.
- (18) Zhou, G.; Li, M.; Li, Y.; Dong, H.; Sun, D.; Liu, X.; Xu, L.; Tian, Z.; Tang, Y. Regulating the Electronic Structure of CoP Nanosheets by O Incorporation for High-Efficiency Electrochemical Overall Water Splitting. *Adv. Funct. Mater.* **2020**, *30* (7), No. 1905252. Liu, C.; Zhang, G.; Yu, L.; Qu, J.; Liu, H. Oxygen Doping to Optimize Atomic Hydrogen Binding Energy on NiCoP for Highly Efficient Hydrogen Evolution. *Small* **2018**, *14* (22), No. 1800421, DOI: 10.1002/smll.201800421.
- (19) Niu, S.; Jiang, W.-J.; Wei, Z.; Tang, T.; Ma, J.; Hu, J.-S.; Wan, L.-J. Se-Doping Activates FeOOH for Cost-Effective and Efficient Electrochemical Water Oxidation. *J. Am. Chem. Soc.* **2019**, *141* (17), 7005–7013. Duan, S.; Chen, S.; Wang, T.; Li, S.; Liu, J.; Liang, J.; Xie, H.; Han, J.; Jiao, S.; Cao, R.; Wang, H.; Li, Q. Elemental selenium enables enhanced water oxidation electrocatalysis of NiFe layered double hydroxides. *Nanoscale* **2019**, *11* (37), 17376–17383.
- (20) Wang, Z.; Liu, H.; Ge, R.; Ren, X.; Ren, J.; Yang, D.; Zhang, L.; Sun, X. Phosphorus-Doped Co<sub>3</sub>O<sub>4</sub> Nanowire Array: A Highly Efficient Bifunctional Electrocatalyst for Overall Water Splitting. *ACS Catal.* **2018**, *8* (3), 2236–2241. Masa, J.; Weide, P.; Peeters, D.; Sinev, I.; Xia, W.; Sun, Z.; Somsen, C.; Muhler, M.; Schuhmann, W. Amorphous Cobalt Boride (Co<sub>2</sub>B) as a Highly Efficient Nonprecious Catalyst for Electrochemical Water Splitting: Oxygen and Hydrogen Evolution. *Adv. Energy Mater.* **2016**, *6* (6), No. 1502313.
- (21) Men, Y.; Li, P.; Yang, F.; Cheng, G.; Chen, S.; Luo, W. Nitrogen-doped CoP as robust electrocatalyst for high-efficiency pH-universal hydrogen evolution reaction. *Appl. Catal., B* **2019**, *253*, 21–27.
- (22) Cao, E.; Chen, Z.; Wu, H.; Yu, P.; Wang, Y.; Xiao, F.; Chen, S.; Du, S.; Xie, Y.; Wu, Y.; Ren, Z. Boron-Induced Electronic-Structure Reformation of CoP Nanoparticles Drives Enhanced pH-Universal Hydrogen Evolution. *Angew. Chem., Int. Ed.* **2020**, *59* (10), 4154–4160.
- (23) Huang, Y.; Li, M.; Pan, F.; Zhu, Z.; Sun, H.; Tang, Y.; Fu, G. Plasma-induced Mo-doped Co<sub>3</sub>O<sub>4</sub> with enriched oxygen vacancies for electrocatalytic oxygen evolution in water splitting. *Carbon Energy* **2023**, *5* (3), No. e279.
- (24) Nguyen, A. D.; Nguyen, T. K.; Le, C. T.; Kim, S.; Ullah, F.; Lee, Y.; Lee, S.; Kim, K.; Lee, D.; Park, S.; Bae, J.-s.; Jang, J. I.; Kim, Y. S. Nitrogen-plasma-treated continuous monolayer MoS<sub>2</sub> for improving hydrogen evolution reaction. *ACS Omega* **2019**, *4* (25), 21509–21515.
- (25) Fan, H.; Huang, X.; Shang, L.; Cao, Y.; Zhao, Y.; Wu, L.-Z.; Tung, C.-H.; Yin, Y.; Zhang, T. Controllable Synthesis of Ultrathin Transition-Metal Hydroxide Nanosheets and their Extended Composite Nanostructures for Enhanced Catalytic Activity in the Heck Reaction. *Angew. Chem., Int. Ed.* **2016**, *55* (6), 2167–2170.
- (26) Xue, Y.; Wang, Y.; Liu, H.; Yu, X.; Xue, H.; Feng, L. Electrochemical oxygen evolution reaction catalyzed by a novel nickel–cobalt–fluoride catalyst. *Chem. Commun.* **2018**, *54* (48), 6204–6207.
- (27) Han, X.; Wu, X.; Deng, Y.; Liu, J.; Lu, J.; Zhong, C.; Hu, W. Ultrafine Pt Nanoparticle-Decorated Pyrite-Type CoS<sub>2</sub> Nanosheet Arrays Coated on Carbon Cloth as a Bifunctional Electrode for Overall Water Splitting. *Adv. Energy Mater.* **2018**, *8* (24), No. 1800935.
- (28) Lu, Q.; Hutchings, G. S.; Yu, W.; Zhou, Y.; Forest, R. V.; Tao, R.; Rosen, J.; Yonemoto, B. T.; Cao, Z.; Zheng, H.; Xiao, J.; Jiao, F.; Chen, J. Highly porous non-precious bimetallic electrocatalysts for efficient hydrogen evolution. *Nat. Commun.* **2015**, *6* (1), No. 6567. Yang, L.; Zhou, W.; Hou, D.; Zhou, K.; Li, G.; Tang, Z.; Li, L.; Chen, S. Porous metallic MoO<sub>2</sub>-supported MoS<sub>2</sub> nanosheets for enhanced electrocatalytic activity in the hydrogen evolution reaction. *Nanoscale* **2015**, *7* (12), 5203–5208.
- (29) Xu, K.; Cheng, H.; Lv, H.; Wang, J.; Liu, L.; Liu, S.; Wu, X.; Chu, W.; Wu, C.; Xie, Y. Controllable Surface Reorganization Engineering on Cobalt Phosphide Nanowire Arrays for Efficient Alkaline Hydrogen Evolution Reaction. *Adv. Mater.* **2018**, *30* (1), No. 1703322.
- (30) Zhou, Q.; Shen, Z.; Zhu, C.; Li, J.; Ding, Z.; Wang, P.; Pan, F.; Zhang, Z.; Ma, H.; Wang, S.; Zhang, H. Nitrogen-Doped CoP Electrocatalysts for Coupled Hydrogen Evolution and Sulfur Generation with Low Energy Consumption. *Adv. Mater.* **2018**, *30* (27), No. 1800140.
- (31) He, W.; Han, L.; Hao, Q.; Zheng, X.; Li, Y.; Zhang, J.; Liu, C.; Liu, H.; Xin, H. L. Fluorine-Anion-Modulated Electron Structure of Nickel Sulfide Nanosheet Arrays for Alkaline Hydrogen Evolution. *ACS Energy Lett.* **2019**, *4* (12), 2905–2912.
- (32) Liu, X.; Meng, J.; Zhu, J.; Huang, M.; Wen, B.; Guo, R.; Mai, L. Comprehensive Understandings into Complete Reconstruction of Precatalysts: Synthesis, Applications, and Characterizations. *Adv. Mater.* **2021**, *33* (32), No. 2007344.
- (33) Zhang, B.; Jiang, K.; Wang, H.; Hu, S. Fluoride-induced dynamic surface self-reconstruction produces unexpectedly efficient oxygen-evolution catalyst. *Nano Lett.* **2019**, *19* (1), 530–537.
- (34) Kou, Z.; Yu, Y.; Liu, X.; Gao, X.; Zheng, L.; Zou, H.; Pang, Y.; Wang, Z.; Pan, Z.; He, J.; Pennycook, S. J.; Wang, J. Potential-Dependent Phase Transition and Mo-Enriched Surface Reconstruction of  $\gamma$ -CoOOH in a Heterostructured Co-Mo<sub>2</sub>C Precatalyst Enable Water Oxidation. *ACS Catal.* **2020**, *10* (7), 4411–4419. Yao, N.; Wang, G.; Jia, H.; Yin, J.; Cong, H.; Chen, S.; Luo, W. Intermolecular Energy Gap-Induced Formation of High-Valent Cobalt Species in CoOOH Surface Layer on Cobalt Sulfides for Efficient Water Oxidation. *Angew. Chem., Int. Ed.* **2022**, *61*, No. e202117178.
- (35) Xie, Y.; Zhao, B.; Tang, K.; Qin, W.; Tan, C.; Yao, J.; Li, Y.; Jiang, L.; Wang, X.; Sun, Y. In-situ phase transition induced nanoheterostructure for overall water splitting. *Chem. Eng. J.* **2021**, *409*, No. 128156.